Systems/Circuits

Transformation of Motion Pattern Selectivity from Retina to Superior Colliculus

Victor J. DePiero,[1,2*] Zixuan Deng,[3*] Chen Chen,[2] Elise L. Savier,[1,4] Hui Chen,[1,2] Wei Wei,[5] and Jianhua Cang[1,2]
[1]Department of Biology, [2]Department of Psychology, University of Virginia, Charlottesville, Virginia 22904, [3]Committee on Neurobiology, University of Chicago, Chicago, Illinois 60637, [4]Department of Physiology, University of Michigan, Ann Arbor, Michigan 48109, and [5]Department of Neurobiology, Neuroscience Institute, University of Chicago, Chicago, Illinois 60637

The superior colliculus (SC) is a prominent and conserved visual center in all vertebrates. In mice, the most superficial lamina of the SC is enriched with neurons that are selective for the moving direction of visual stimuli. Here, we study how these direction selective neurons respond to complex motion patterns known as plaids, using two-photon calcium imaging in awake male and female mice. The plaid pattern consists of two superimposed sinusoidal gratings moving in different directions, giving an apparent pattern direction that lies between the directions of the two component gratings. Most direction selective neurons in the mouse SC respond robustly to the plaids and show a high selectivity for the moving direction of the plaid pattern but not of its components. Pattern motion selectivity is seen in both excitatory and inhibitory SC neurons and is especially prevalent in response to plaids with large cross angles between the two component gratings. However, retinal inputs to the SC are ambiguous in their selectivity to pattern versus component motion. Modeling suggests that pattern motion selectivity in the SC can arise from a nonlinear transformation of converging retinal inputs. In contrast, the prevalence of pattern motion selective neurons is not seen in the primary visual cortex (V1). These results demonstrate an interesting difference between the SC and V1 in motion processing and reveal the SC as an important site for encoding pattern motion.

Key words: **patch clamp; plaids; superior colliculus; two-photon imaging; visual system**

Significance Statement

An important function of the visual system is to encode the direction of complex motion patterns in the environment. Studies using the plaid stimulus have revealed neurons in different cortical areas that are tuned to either pattern motion or component motion, but how neurons in the SC respond to plaids has not been studied. Here, we show that direction selective neurons in the mouse SC respond to plaids with a clear pattern motion selectivity, at a level not seen in the retina or V1. Our results thus provide new information regarding the function and organization of the early visual system and highlight the importance of SC circuits in computing complex motion.

Received Sept. 11, 2023; revised March 7, 2024; accepted March 26, 2024.

Author contributions: V.J.D., H.C., W.W., and J.C. designed research; V.J.D., Z.D., C.C., and E.L.S. performed research; V.J.D., Z.D., C.C., E.L.S., H.C., and W.W. analyzed data; V.J.D. and J.C. wrote the paper.

We thank Dr. Seiji Tanabe and other members of the Cang lab for discussion and comments on the manuscript. We also thank Dr. Manavu Tohmi for his help with intrinsic imaging and Chen Zhang for managing the mouse colony in the Wei lab. We thank Dr. Stephanie M Palmer, Dr. John Maunsell, Yunlong Xu, and members of the Wei Lab for helpful discussions. This work was supported by the Pritzker Fellowship and NIDA Training Grant R90DA 060338 to Z.D, US National Institutes of Health (NIH) grants (EY026286 and EY020950 to J.C. and NS109990 to W.W.), and Jefferson Scholars Foundation to J.C.

*V.J.D. and Z.D. contributed equally to this work.

The authors declare no competing financial interests.

Correspondence should be addressed to Jianhua Cang at cang@virginia.edu or Wei Wei at weiw@uchicago.edu.

https://doi.org/10.1523/JNEUROSCI.1704-23.2024

Introduction

Detecting moving objects in the environment is an important function of the visual system. Neurons that respond selectively to visual motion, especially to its moving directions, are seen throughout the visual system, from the retina to the primary visual cortex (V1) and higher cortical area MT (Nishida et al., 2018; Wei, 2018; Pasternak and Tadin, 2020). Simple visual stimuli such as moving bars and drifting gratings are routinely used to study direction selectivity and its underlying mechanisms (Vaney et al., 2012; Mauss et al., 2017). More complex motion patterns, including the so-called plaids, have also proved useful in studying how neuronal populations in different visual areas

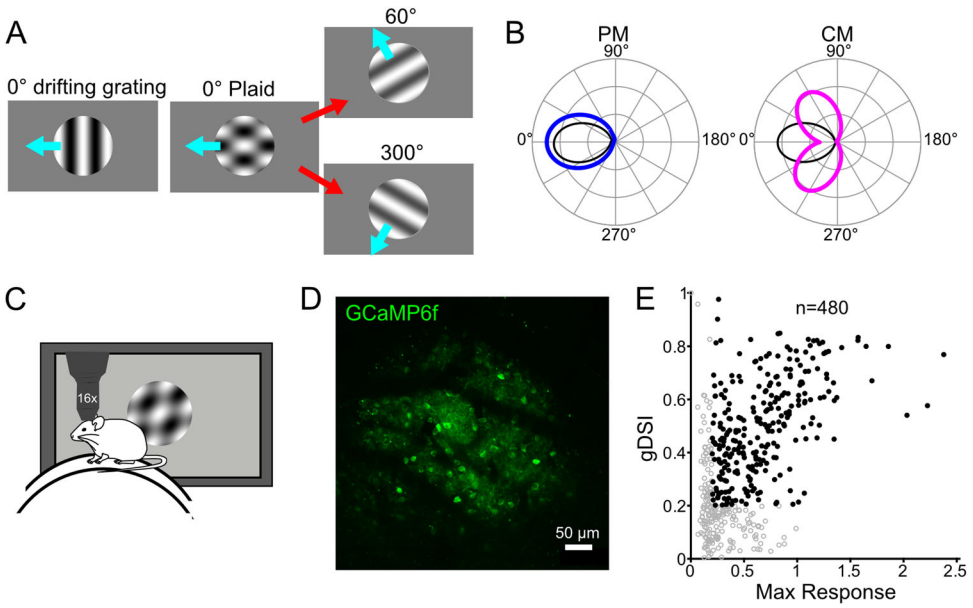

Figure 1. Experimental design. ***A***, Examples of presented drifting gratings and plaid visual stimulus. Left, a sinusoidal drifting grating. The cyan arrow shows its direction of movement on the screen that corresponds to 0° or forward motion from the animal's perspective. Middle, a plaid stimulus with the cyan arrow showing the perceived 0° direction. Right, red arrows from the example plaid point to the component sinusoidal gratings. For the 0° plaid, with a 120° cross angle, this means 60° (top) and 300° (bottom) drifting gratings. ***B***, Predicted tuning curves of a pattern motion (PM) selective cell (left) and component motion (CM) selective cell (right). The black curve is the tuning curve of a hypothetical neuron that is tuned to a 0° drifting grating. The blue tuning curve represents the predicted response to plaids if it were PM selective, whereas the magenta curve represents the predicted CM response. ***C***, Schematic of the two-photon imaging setup. The stimulus screen was placed on the side contralateral to the imaging window at the retinotopic location that best corresponded to the imaged field of view. The mouse was free to run on a cylindrical wheel. ***D***, Image of neurons in the superficial SC (sSC) labeled with GCaMP6f. Scale bar: 50 µm. ***E***, Scatter plot of all the visually responsive sSC neurons showing gDSI versus max response, $n = 480$ neurons from 8 mice. Solid black circles represent responsive neurons that passed the analysis criteria (max $\Delta F/F > 0.2$ and gDSI > 0.2) and open gray circles represent neurons that did not meet the response criteria.

encode motion directions (Adelson and Movshon, 1982). The plaid consists of two superimposed sinusoidal gratings, with orientations separated by a cross angle (Fig. 1*A*). Each grating moves perpendicular to its orientation axis at a constant velocity (Quaia et al., 2016), which gives the perception of motion in a direction that lies between directions of the two gratings (Albright and Stoner, 1995). The discrepancy between the physical characteristic of a plaid and its perceptual characteristic provides an excellent test for evaluating whether individual visual neurons encode the direction of the plaid pattern or its components.

Studies using plaids have revealed a hierarchical organization of motion processing in cortical areas (Adelson and Movshon, 1982; Rodman and Albright, 1989; Quaia et al., 2022). Direction selective neurons in primate V1 tend to show two peaks in their tuning curves to plaids, corresponding to the preferred direction in response to the two component gratings (Fig. 1*B*) (Movshon and Newsome, 1996). In other words, these neurons are tuned to component motion (CM). In contrast, many neurons in the MT, a later stage in cortical processing, are selective for pattern motion (PM), showing a single peak to the plaid at their preferred direction (Fig. 1*B*) (Wang and Movshon, 2016). Modeling studies demonstrated that the PM selectivity can be generated by combining the signals transmitted by the early-stage CM-selective V1 neurons (Rust et al., 2006), supporting the notion of hierarchy. Recent studies in mice have reported both CM- and PM-selective neurons in V1 and higher visual areas (Juavinett and Callaway, 2015; Palagina et al., 2017). Although the exact proportions of the two populations appeared to be quite different from those in primates, still more PM neurons were seen in higher areas than in V1 (Juavinett and Callaway, 2015).

In contrast to the many studies of cortical neurons, plaids have not been used in studies of the superior colliculus (SC), a prominent center for motion processing in the mammalian visual system. The SC, also known as the optic tectum, is a conserved brain structure found in all vertebrates (Basso and May, 2017; Basso et al., 2021). Direction selective neurons have been reported in all species that have been studied, suggesting that they may serve a significant function in visual processing (Cang et al., 2018). In mice, the SC receives input from roughly 85% of retinal ganglion cells (Ellis et al., 2016), a much larger proportion than the proportion projecting to the geniculocortical pathway. We have previously shown that the most superficial lamina of the SC is enriched with direction selective neurons (Inayat et al., 2015; Barchini et al., 2018; Savier et al., 2019), which inherit their selectivity from the precise convergence of retinal direction selective ganglion cells (DSGCs) (Shi et al., 2017). However, whether SC neurons encode CM or PM of the plaid stimulus remains unknown.

Here, using two-photon calcium imaging in awake mice, we find that most direction selective neurons in the superficial SC, but not V1, respond robustly to plaid patterns with a clear PM selectivity. In contrast, DSGCs show ambiguous selectivity. Modeling suggests that PM selectivity in the SC can arise from nonlinear integration of converging retinal inputs. Our data thus demonstrate that PM selectivity is computed early in the visual system, at a stage separate from the cortical hierarchy of motion processing that has been more widely studied.

Materials and Methods

Animals. Adult wild-type C57BL/6 mice and transgenic mice, both males and females, 2–6 months old unless otherwise stated, were used in this study. These included nine wild-type for bulk of the two-photon calcium imaging of SC, and two offspring of crossing *Gad2*-IRES-Cre mice (The Jackson Laboratory, stock #010802, RRID, IMSR_JAX:01080)

with Ai9 reporter (RCL-tdT, stock #007909; RRID, IMSR_JAX:007909). The mice for V1 imaging were obtained by crossing Ai9 reporter with *Vip*-IRES-Cre ($n = 2$, stock #010908; RRID, IMSR_JAX:010908) or Sst-IRES-Cre ($n = 3$, stock #013044; RRID, IMSR_JAX:013044). For retinal electrophysiological recordings, *Drd4-GFP* mice of ages postnatal day 30 (P30) to 60 (P60) of either sex were used to label On-Off DSGCs that prefer motion in the posterior direction (i.e., pDSGCs; Huberman et al., 2009). The *Drd4-GFP* mouse line was originally developed by Mutant Mouse Resource & Research Centers (MMRRC; http://www.mmrrc.org/strains/231/0231.html). For retinal two-photon calcium imaging, Vglut2-ires-Cre knock-in mice (stock #028863, RRID, IMSR_JAX:028863) were crossed with floxed GCaMP6f Ai95 reporter line (stock #028865, RRID, IMSR_JAX:028865). Mice of ages P19–P30 of either sex were used. All mice were kept on a 12/12 h light/dark cycle, with two to five animals housed per cage. All experimental procedures were approved by the University of Virginia or the University of Chicago Institutional Animal Care and Use Committee and in conformance with the National Institutes of Health *Guide for the Care and Use of Laboratory Animals* and the Public Health Service Policy.

SC and V1 surgery for in vivo imaging. SC and V1 surgeries and recordings were performed as described in (Savier et al., 2019). Briefly, the mouse was anesthetized with isoflurane (5% for induction) and place on a heating pad in a stereotaxic surgery station (Digital Model 1900, Stereotaxic Alignment System, Kopf Instruments) and continuously given isoflurane and oxygen (2.5% for maintenance, in O_2, ~0.5 L/min; VetFlo, Kent Scientific). The head was shaved, and the scalp cut to expose the skull. To image the posterior and medial portion of the SC, a 2.5 mm craniotomy was centered over lambda point and the skull fragments were carefully removed. The dura over the colliculus was cut with a sharp needle (30 gauge) to expose the left hemisphere without lesioning the cortex.

A glass pipette fitted to an injector, (Drummond Scientific Nanoject II) was loaded with a 1.5 µl of AAV1-hsyn-GCaMP6f-WPRE-SV40 (Addgene #100837) and inserted 500 µm below the pia surface of SC and ~50 nl was injected. The injector was moved up to 250 µm and another ~50 nl of the viral vector was injected. The injection procedure was repeated at another location approximately 250 µm lateral to the first injection site. Next, a custom-made cranial window was inserted to push cortex away from the SC and glued in place using Vetbond (3 M). Finally, a titanium head plate and ring were fixed to the skull using Metabond (Parkell) mixed with black ink. The animal was given carprofen (5 mg/kg), subcutaneously, and left to recover on a heating pad for 30 min or until ambulatory before being placed back in its home cage.

To image the anterior portion of the SC, we used a surgery similar to that described in (de Malmazet et al., 2018). A 3.2 mm craniotomy was performed on the left hemisphere centered 1.5–2 mm vertical and horizontal from lambda point. The cortex above the SC was aspirated using a pipette tip and low vacuum. Once the SC was exposed, injections of AAV1-hsyn-GCaMP6s-WPRE-SV40 (Addgene #100843) were made at depths as described above. A 3 mm diameter and 2.75 mm long stainless-steel cannula with a glass window at one end was inserted and fixed to the skull using Metabond. Animals had headplates affixed to the skull and were left to recover as described above.

For V1 imaging, a similar surgery was performed but differed in the location of the craniotomy and injection sites. A 2.5 mm in diameter craniotomy was performed 2.3 mm lateral from the midline and along the lambda suture in the left hemisphere. A glass pipette was loaded with AAV1-hsyn-GCaMP6f-WPRE-SV40 viral vector. The pipette was lowered into the V1 to 500 µm deep as the first injection depth, and then retracted back to 250 µm below surface as the second depth. At each depth, a total volume of ~50 nl was slowly delivered, in 10 pulses. Three sites were injected of each mouse across the latero-medial axis, 2.0 mm, 2.3 mm, and 2.6 mm from the midline and near the lambda suture. Headplate fixation and recovery procedures were the same as SC surgery. To confirm receptive field location in V1 surgery animals, we used wide-field imaging (Tohmi et al., 2021). A binocular microscope (MVX10, Olympus) equipped with a 0.63×, 0.15 NA objective (MV PLAPO, Olympus), an Olympus U-M49002XL filter cube (excitation filter, 470/40 nm; dichroic mirror, 495 nm high pass; emission filter, 525/50 nm) and a CCD-camera (BU-61 M, Bitran), was used to record calcium signals. The mice were head-fixed and awake. The V1 surface was excited with a 470 nm LED (UHP-T-LA, Prizmatix) of ~4.2 mW below the objective. Images (240 × 135 pixels) were recorded at 10 Hz with custom acquisition software (LabVIEW 2017, National Instrument).

In vivo two-photon imaging and visual stimulation. Imaging started 15–21 d postsurgery under a two-photon scanning microscope (Ultima Investigator, Bruker Nano Surface Division) with a Ti:sapphire laser (Chameleon Discovery with TPC, Coherent) tuned to a wavelength of 920 nm using a 16×, 0.8 NA Nikon objective. Imaging data were acquired using the PrairieView software (version 5.4) with a resonant scanner at 2.25× optical zoom, resulting in a 412.2 × 412.2 µm field of view (at 512 × 512 pixel resolution). The data acquisition rate was 30 Hz, and four-frame averages were used for image analysis.

During imaging, mice were head-fixed on a cylindrical wheel. Visual stimuli were generated with MATLAB Psychophysics toolbox (Brainard, 1997) on an LCD monitor (59.7 × 33.6 cm, Samsung C27F398FW 60 Hz refresh rate, ~50 cd/m^2 mean luminance, gamma corrected). The screen was placed 25 cm away from the eye contralateral to the imaging site (the right eye for both SC and V1 experiments). The monitor was moved for every imaged field-of-view so that the cells' receptive fields were near the center of the screen.

For SC imaging, sinusoidal drifting gratings (100% contrast; spatial frequency 0.08 cycle per degree or cpd, unless otherwise stated; temporal frequency 2 Hz) were presented on a gray background in a circular patch (40° diameter) at the center of the screen. 12 different directions were used, ranging from 0° to 330° and tiling all direction space in 30° increments. The 0° represented forward motion (temporal-to-nasal) from the animal's perspective. A blank (gray) condition was added to the 12 directions. Each stimulus condition of the gratings was presented for 1 s, followed by a gray screen for 3 s. The entire stimulus set was shown to the mouse ten times in a pseudorandom fashion for every imaged field of view. For V1 imaging, 60° diameter sinusoidal drifting grating of 12 directions were presented in a pseudo-randomized fashion (1 s stimuli, 3 s gray screen wait interval, 2 Hz, 0.04 cpd).

Type I plaids were used in this study, in which the two component gratings are symmetric and the resulting direction of the global pattern is exactly at the middle of the two grating directions (Fig. 1*A*). The plaid stimulus consisted of two sinusoidal drifting gratings of 50% contrast superimposed over one another on a gray background (Fig. 1*A*,*C*). The cross angle of the two gratings was either 60°, 90° or 120°. The parameters of the two superimposed drifting gratings were the same (40° diameter, 2 Hz, 0.08 cpd for SC and 60° diameter, 2 Hz, 0.04 cpd for V1). Plaids were presented the same way as for drifting gratings, 12 directions, 1 s stimulus presentation followed by 3 s gray screen.

The timing and parameters of each presented visual stimulus were recorded by the PrairieView software simultaneously with the imaging data. Onset and offset of the visual stimulus were recorded in a third channel (in addition to red and green channels) to ensure synchronization of the stimulus presentation and image scan. Stimulus conditions were encoded in transistor-to-transistor (TTL) pulses.

Whole-mount retina preparation for ganglion cell patch clamp recording and visual stimulation. Mice were dark adapted for >30 min, anesthetized with isoflurane and then euthanized by decapitation. Under infrared light, retinas were isolated from the pigment epithelium layer and cut into halves at room temperature in Ames' medium (bubbled with 95% O_2/5% CO_2; Sigma-Aldrich). The retinas were then mounted with ganglion cell layer up on top of a ~1.5 mm^2 hole in a small piece of filter paper (Millipore). Cells in the center of the hole were used for experiments. Throughout the experiment, tissues were kept in the darkness except during visual stimulation, and brief two-photon imaging to find the GFP-expressing cells (<10 s scanning time with a 920 nm pulse laser (Coherent) for each cell).

A white organic light-emitting display (OLED; 800 × 600 pixel resolution, delivered to the retina with a scale factor of 1.1 µm/pixel, 60 Hz refresh rate, 470–620 nm; OLEDXL, eMagin) was controlled by an

Intel Core Duo computer with a Windows 7 operating system and presented to the retina. The OLED visual stimuli were generated using MATLAB and Psychophysics Toolbox. Sinusoidal drifting gratings (300 μm/∼10° in diameter; 0.15 cpd; 2 Hz; stimulus presentation for 3 s; interstimulus interval for 2 s) were presented moving in 12 directions with 3 repetitions each. Plaids were constructed by superimposing two sinusoidal gratings of equal contrast, moving at the same spatial and temporal frequency.

Retinas were perfused with oxygenated Ames' medium with a bath temperature of 32–34°C. GFP-labeled pDSGCs in *Drd4-GFP* mice were targeted using a two-photon microscope (Bruker Nano) and a Ti: sapphire laser (Coherent) tuned to 920 nm. Data were acquired using PCLAMP 10 software, a Digidata 1550A digitizer, and a MultiClamp 700B amplifier (Molecular Devices); low-pass filtered at 4 kHz; and digitized at 10 kHz. For cell-attached recordings, electrodes of 3.5–5 MΩ were filled with Ames' medium (Sigma-Aldrich).

Two-photon calcium imaging of RGC visual responses. GCaMP6f fluorescence of isolated retinas in oxygenated Ames at 32−33°C was imaged in a customized two-photon laser scanning fluorescence microscope (Bruker Nano Surfaces Division). GCaMP6f was excited by a Ti: sapphire laser (Coherent, Chameleon Ultra II) tuned to 920 nm, and the laser power was adjusted to avoid saturation of the fluorescent signal. Onset of laser scanning induces a transient two-photon response that adapts to the baseline in 3 s. Therefore, to ensure the complete adaptation of this laser-induced response and a stable baseline, visual stimuli were given after 20 s of continuous laser scanning. To separate the visual stimulus from GCaMP6f fluorescence, a band-pass filter (Semrock, Rochester, MA) was placed on the OLED to pass blue light peaked at 470 nm, while two notched filters (Bruker Nano Surfaces Division) were placed before the photomultiplier tubes to block light of the same wavelength. The objective was a water immersion objective (20×, Olympus). Time series of each imaging window were collected at 10 Hz or higher.

Similar to electrophysiology recording, sinusoidal drifting gratings (660 μm/∼22° in diameter; 0.15 cpd; 2 Hz; stimulus presentation for 2 s; interstimulus interval for 2 s) were presented moving in 12 directions with 5 repetitions each. Plaids were constructed by superimposing two sinusoidal gratings of equal contrast, moving at the same spatial and temporal frequency. A TTL pulse is sent at the beginning and end of each stimulus direction to ensure synchronization of the stimulus presentation and image scan. For a given field of view, responses to gratings, plaids, and stationary spots were collected in separate imaging blocks with at least 2 min rest in between.

SC and V1 calcium imaging data analysis. We followed our published procedures to analyze the imaging data (Inayat et al., 2015; Barchini et al., 2018; Savier et al., 2019; Chen et al., 2021). Briefly, regions of interest (ROIs) were manually drawn on the average image of a population of neurons averaged over the collected time-series, and the intensity values of all pixels in each ROI were averaged for each frame to obtain raw Ca^{2+} signal. From the raw fluorescence trace, $\Delta F/F0 = (F - F0)/F0$ was calculated, where F0 was the mean of the baseline signal over six frames before stimulus onset, and F was the average fluorescence signal over eight frames, starting from one frame after stimulus onset. A cell was considered responsive if its mean ΔF/F0 was >2 SDs above its F0 for at least one stimulus condition. The mean value of ΔF/F0 for each stimulus condition was then used for subsequent data analysis for all the responsive cells.

To quantify the degree of direction selectivity, we calculated the vector sum, of the fluorescent responses normalized to the scalar sum, referred to as the global direction selective index (gDSI; Gale and Murphy 2014; Inayat et al., 2015) as follows:

$$\mathrm{gDSI} = \left|\frac{\sum R_\theta e^{i\theta}}{\sum R_\theta}\right|,$$

where R_θ is the response magnitude in ΔF/F0 at a stimulus direction θ (in radians). The preferred direction was the angle of the vector summation in degrees. We similarly calculated the global orientation selective index (gOSI) using the following:

$$\mathrm{gOSI} = \left|\frac{\sum R_\theta e^{i2\theta}}{\sum R_\theta}\right|.$$

The maximum response for each selected ROI was determined as the largest ΔF/F0 value among all stimulus conditions.

Categorization of responses into CM selective, PM selective, or unclassified was computed similarly to previous studies (Smith et al., 2005; Juavinett and Callaway, 2015; Palagina et al., 2017). First, for each cell, we generated the predicted pattern and component tuning curves based on the tuning curves of the responses to drifting gratings. We next calculated the Pearson correlation coefficients between the observed responses to the plaid and the predicted values for the pattern responses (P) and component responses (C), as well as the Pearson correlation coefficients between the predicted pattern and predicted component values (PC). Then we calculated an adjusted partial correlation coefficient for both pattern:

$$\mathrm{RP} = \frac{\mathrm{P} - \mathrm{C} \times \mathrm{PC}}{\sqrt{((1 - \mathrm{C}^2) * (1 - \mathrm{PC}^2)}},$$

and component selectivity:

$$\mathrm{RC} = \frac{\mathrm{C} - \mathrm{P} \times \mathrm{PC}}{\sqrt{((1 - \mathrm{P}^2) \times (1 - \mathrm{PC}^2)}}.$$

Next, using the Fisher *z*-score transformation (Smith et al., 2005), we calculated the *z*-score values of RP and RC for each neuron:

$$\mathrm{ZP} = 1.5 \times \ln\left(\frac{1 + \mathrm{RP}}{1 - \mathrm{RP}}\right); \quad \mathrm{ZC} = 1.5 \times \ln\left(\frac{1 + \mathrm{RC}}{1 - \mathrm{RC}}\right).$$

The number of degrees of freedom (1.5) is calculated using $\sqrt{n-3} \times 0.5$ where n is the number of stimuli directions ($n = 12$). These calculated z-scores when bounded by 95% confidence interval of 1.645 allow us to classify neurons into PM, CM, and unclassified. The 95% confidence boundary lines for the adjusted correlation coefficients (RC and RP) were calculated as follows:

$$\mathrm{RP} > \frac{-1 - \mathrm{RC} + b - b * \mathrm{RC}}{-1 - \mathrm{RC} - b + b * \mathrm{RC}}; \quad \mathrm{RC} < \frac{-1 + \mathrm{RP} + b + b * \mathrm{RP}}{1 - \mathrm{RP} + b + b * \mathrm{RP}}; \text{ where } b = \log\left(e^{2 \times 1.645/\sqrt{n-3}}\right).$$

Retina calcium imaging data analysis. Analysis was performed using ImageJ, Suite2p, and MATLAB. For a given field of view, frames from gratings stimuli were run through Suite2p to perform motion correction, region of interest (ROI) detection and raw fluorescence extraction. ROIs were manually curated using the Suite2p GUI to retain only those corresponding to somas. Raw frames were also uploaded onto ImageJ software in which a background region was manually selected where there was no detectable GCaMP6f expression. The raw fluorescence and background were then imported into MATLAB, where custom written scripts were used to calculate the average intensity over time for all ROIs. Background trace was smoothed using a moving average of 10 data points (∼1 s) and subtracted from the light responsive somatic traces to remove noise. The background subtracted raw fluorescence traces (F) were then checked to ensure they had a stable baseline fluorescence in the absence of visual stimulation. They were then clipped according to TTL pulse into 4 s intervals (2 s of stimulus presentation followed by 2 s of gray screen). For each interval, $\Delta F = F - F0$ was calculated, where F0 was the mean of the lowest 8 data points (∼800 msec) during each interval. This ensures that baseline drift has minimal effect on ΔF. The mean value of ΔF across time was used for subsequent analysis, and the integral value of ΔF for each interval was then used as response

magnitude at each stimulus direction θ. Prior to further analysis, traces were subjected to a response quality test, QI = Var[⟨C⟩r]t/⟨Var[C]t⟩r (Baden et al., 2016), to ensure consistency across trials. The quality index is calculated as the variance of mean response over time divided by the mean variance over time across stimulus repetitions. C is the time samples by stimulus repetition matrix for each ROI, ⟨⟩ and Var[ ] denotes the mean and variance across the indicated dimension. Each ROI is manually inspected and repetitions with drift in *z*-direction are excluded. We implemented a quality threshold of QI 0.12 for the response from a given cell to be considered for further analysis.

We then quantified the degree of direction selectivity and selected direction selective ROIs (gDSI > 0.2, see above methods). Only DS ROIs identified using gratings were used for subsequent analysis. Each DS somas was manually identified and matched in image stacks for plaids and spots, where we extract the background-subtracted raw fluorescence for selected ROIs. We separate the DS ROIs into ON and On-Off classes based on their response to stationary flashed spots (660 μm/∼22° in diameter; 4 s prestimulus wait; 1 s on; 1 s off; 3 repetitions). A cell is considered On-Off if its ΔF during the OFF period was >2 SD above its baseline fluorescence F0 for at least one repetition. F0 is quantified as the mean of the fluorescence signal during 4 s of prestimulus time. A cell is otherwise considered ON due to its response during the ON period of grating stimuli. Traces from DS ROIs matched for plaids were subject to the same quality test. A given cell with both grating and plaid response passing quality threshold were categorized as CM, PM or unclassified using the before-mentioned methods.

Modeling. To model the transformation from retina to the SC, we used DSGC spike recordings as input to avoid additional input nonlinearity due to calcium dynamics. We used grating and plaid responses from the 90° cross angle, where we had most cells. To estimate the tuning width of each cell, we fit tuning curves with the von Mises distribution (Oesch et al., 2005; Elstrott et al., 2008):

$$R(\theta) = R_{\max}\frac{e^{-k\cos(\theta-\mu)}}{e^{k}},$$

where $R(\theta)$ is the response to motion in a given stimulus direction θ in radians, $R_{\max}$ is the maximum response, μ is the preferred direction in radians, and k is the concentration parameter accounting for tuning width. The tuning width of each cell was quantified as the full-width at half-height (fwhh).

We began modeling by generating normalized tuning curves for individual DSGCs and sSC neurons. Based on a previous study demonstrating the convergence of similarly tuned DSGCs onto individual SC neurons (Shi et al., 2017), we rotated each cell's grating and plaid response in steps of 30° so that the resulting preferred directions to gratings are centered at 180 ± 30°. This preserves the correlation between grating and plaid response for each DSGC and sSC neuron while mimicking expected jitter in experimentally measured retinal input and SC output.

To estimate the mean nonlinearity between retinal input and SC output, we performed a bootstrap analysis. On each iteration of the bootstrap, we randomly drew, with replacement, five DSGCs and one SC neuron. We took the averaged DSGC directional response as input and the directional response of SC neuron as output. We performed 5,000 such iterations and fit a modified sigmoid function where X is binned retinal grating input (100 bins) and Y the corresponding mean sSC response:

$$Y = \frac{L}{1 + e^{-k(X-x0)} + b}.$$

To ensure that the fitted parameters represent the "true" mean nonlinearity of DSGC and sSC grating transformation, we used the mean estimated parameters from 1,000 draws (each consisting of 5,000 iterations). This ensured that any bias resulting from variability in retinal input, random sampling, and SC output was accounted for to capture retina-SC transformation for gratings.

Next, we simulated a population of SC neurons by iteratively drawing 5 DSGCs, averaging their directional response to gratings and plaid, and applying the fitted nonlinearity above to obtain the predicted SC directional response respectively. We then used the analysis methods described above to calculate the *z*-score values of RP and RC for each simulated neuron. To examine the distribution of CM and PM selectivity, we used pattern index, which is calculated as Zp − Zc (Rust et al., 2006).

Statistics. Significance tests were done using Wilcoxon signed rank test for paired data. All analyses and graph plotting were performed in MATLAB (MathWorks; RRID, SCR_001622). No statistical methods were used to predetermine sample sizes, but our sample sizes are similar to those reported in the field. We did not randomly assign animals to groups because it is not applicable to the experimental design of this study.

Results

Direction selective neurons in the mouse SC predominantly show PM selectivity

Using two photon calcium imaging (Fig. 1*C*,*D*), we recorded 671 neurons in the superficial stratum griseum superficiale (SGS), within 100 μm from the collicular surface (Inayat et al., 2015). 480 (71.5%) of those neurons were visually responsive to drifting gratings (Fig. 1*E*, see Materials and Methods for details of responsiveness determination). 278 (57.9%) of the responsive neurons were found to be directional selective (gDSI > 0.2 and max ΔF/F > 0.2) and they were further analyzed for their motion selectivity to plaids. To accommodate for the broad tuning width of direction selective SC neurons (Inayat et al., 2015), we first used a 120° cross angle between the component gratings. Responses to gratings (Fig. 2*A*, solid curves) and plaids (dotted curves) were collected under two separate imaging blocks. Most direction selective neurons in the mouse SC showed remarkably similar tuning curves of responses to gratings and plaids (Fig. 2*A*, blue box), i.e., displaying PM like responses.

To quantify these observations, we compared basic response properties to gratings and plaids for the population of direction selective SC neurons. There was a strong correlation between the maximum responses ($\Delta F/F_0$) to plaids and gratings (Fig. 2*B*; $r^2 = 0.703$, $p = 0.974 \times 10^{-75}$), with significantly stronger responses to plaid stimuli ($p = 3.1 \times 10^{-10}$, z statistic = −6.29, Wilcoxon test). Furthermore, these neurons overall showed highly selective responses to plaids, with their gDSI (Fig. 2*C*; $r^2 = 0.658$, $p = 2.92 \times 10^{-66}$) and preferred direction (Fig. 2*D*; $r^2 = 0.890$, $p = 4.39 \times 10^{-134}$) strongly correlated with those in response to single gratings. These basic features show that direction selective SC neurons respond robustly to complex motion of type I plaids while remaining highly selective for direction.

To test how consistently the neuron's tuning follows PM, we classified SC neuronal responses into PM- and CM-selective responses following the well-established plaid analysis paradigm described in Materials and Methods (Movshon et al., 1985; Movshon and Newsome, 1996; Smith et al., 2005; Juavinett and Callaway, 2015; Palagina et al., 2017). Briefly, for each neuron, we calculated its predicted pattern and component tuning curves based on its responses to drifting gratings. We then calculated the Pearson correlation coefficient between the observed plaid tuning curve and the predicted pattern (and component) responses. These correlation coefficients were used to calculate the adjusted correlation for pattern (Rp) versus component (Rc) responses (see Materials and Methods for details; Fig. 3*B*). Next, we calculated and plotted the *z*-score value using the Fisher *z*-transform

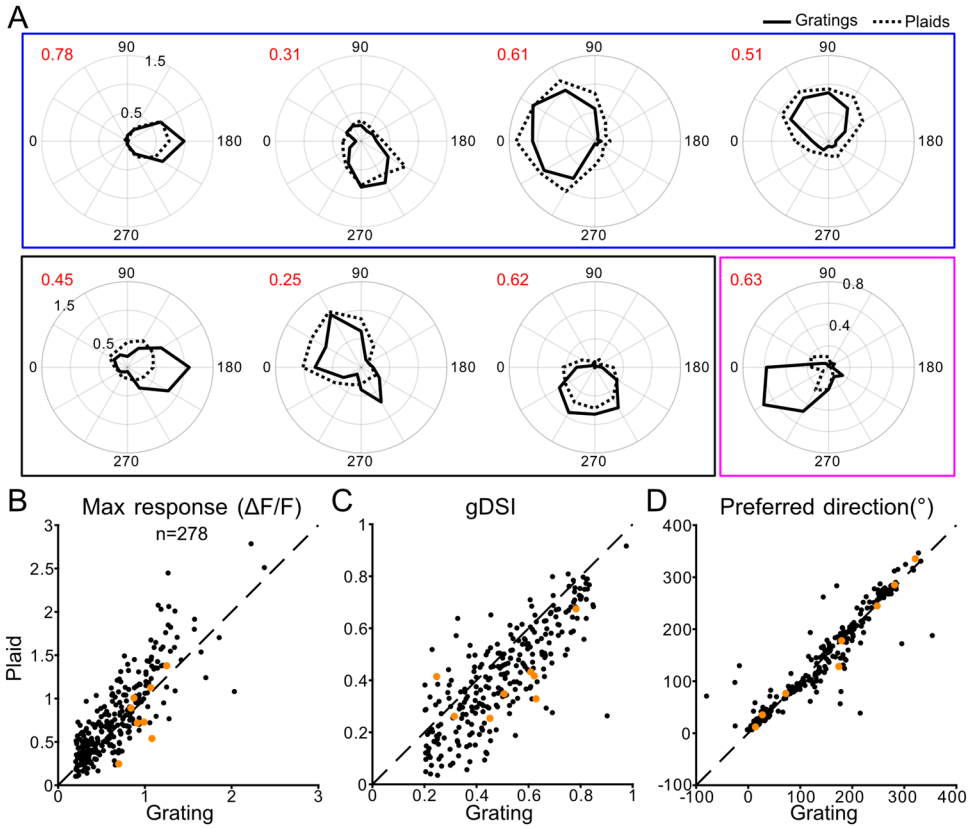

Figure 2. Example tuning curves and response properties of SC neurons to plaids and gratings. ***A***, Example tuning curves of SC neurons. Solid black lines are the response to drifting gratings and the dotted lines are the responses to plaids. Numbers in red are the gDSI to the grating. ***B***, Scatter plot of maximum response for plaids versus drifting gratings. ***C***, Scatter plot of gDSI for plaids versus drifting gratings. ***D***, Scatter plot of the preferred direction of plaid versus gratings. $n = 278/480$ visually responsive SC neurons that met the selection criteria: max $\Delta F/F > 0.2$ and gDSI > 0.2. Dashed black line represents the line of equality. Orange circles in panels B-D correspond to the individual neurons plotted in ***A***.

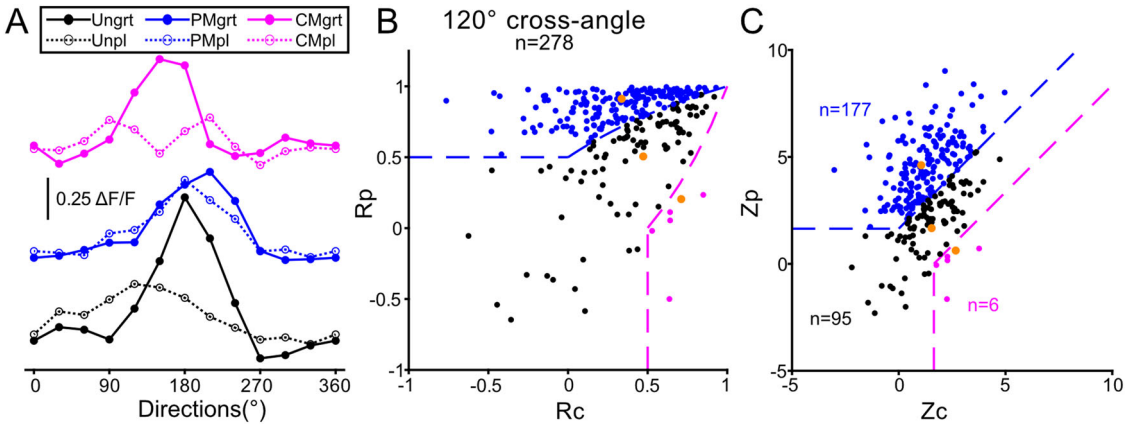

Figure 3. SC neurons are predominantly pattern selective to 120° plaids. ***A***, Example tuning curves of three SC neurons plotted using the Cartesian axis. Solid lines are the responses to drifting gratings and dashed lines are the responses to plaids. Ungrt, Unclassified responses to grating; Unpl, Unclassified responses to plaid; PMgrt, PM responses to grating; PMpl, PM responses to plaid; CMgrt, CM responses to grating; CMpl, CM responses to plaid. ***B***, Scatter plot of partial correlation coefficients (Rp vs Rc). Dashed lines represent the 95% confidence threshold. ***C***, Scatter plot of the *z*-score coefficients (Zp vs Zc). Dashed lines represent 95% confidence threshold. All neurons are colored according to *z*-score statistics classification (blue indicates PM, black indicates unclassified, and magenta indicates CM). The orange circles in ***B*** and ***C***, correspond to the three example neurons shown in ***A***.

(Fig. 3C). Using 95% confidence as a cutoff, we found 63.7% (177/278) of direction selective SC neurons were PM selective, whereas CM-selective SC ones only accounted for 2.2% (6/278). The remaining 34.2% (95/278) were unclassified, meaning that our statistical analysis could not classify them as either PM or CM selective.

Together, these data demonstrated that direction selective neurons of the superficial SC preferentially respond to the perceived motion of the plaid stimuli and not the individual moving components that make up the plaid. This reveals PM-selectivity being computed early in the visual system, presumably separate from the CM-to-PM transformation in the cortex.

Both excitatory and inhibitory sSC neurons show pattern selective responses

Inhibitory neurons account for roughly 60% of the neuronal population in the superficial SC, a significantly higher proportion than found in the cortex (Liu et al., 2023). We thus explored whether the excitatory or inhibitory nature of an SC neuron has any relationship with PM- or CM-selectivity. We tested for this by performing two-photon imaging of SC neurons that expressed GAD2, an inhibitory cell marker, while presenting drifting gratings and plaids.

The series of two-photon images in Figure 4*A* show expression of GCaMP6s (green), expression of tdTomato (red, indicating GAD2 expression) in a subset of neurons, and finally the overlap of the GCaMP6s and tdTomato (yellow). We determined putative inhibitory (GAD2+) neurons from putative excitatory (GAD2−) neurons based on the overlap of green and red fluorescence (Fig. 4*A*, bottom). We recorded responses of 124 neurons to drifting gratings and 120° cross angle plaids, including 80 (64.5%) GAD2+ neurons and 44 (35.5%) GAD2− neurons (Fig. 4*B*).

Z-score analysis showed no difference in distributions of PM and CM selectivity between inhibitory (Fig. 4*B*, left) and excitatory (Fig. 4*B*, right) neurons. Most neurons were PM selective regardless of inhibitory (72.5%, 58/80) or excitatory (61.4%, 27/44) labeling. Furthermore, both excitatory and inhibitory neurons show high direction selectivity to gratings (mean gDSI; excitatory, 0.459 ± 0.023; inhibitory, 0.549 ± 0.019) and the gDSI is correlated between drifting gratings and plaids in both cell types (Fig. 4*C*; inhibitory, $r^2 = 0.641$, $p = 5.09 \times 10^{-19}$; excitatory, $r^2 = 0.498$, $p = 8.66 \times 10^{-8}$).

PM-selective SC responses at wider cross angles

We next examined systematically how SC neurons responded to plaids that were composed of gratings of different cross angles. When the cross angle decreased, from 120° to 90° and to 60°, the *z*-score distribution shifted toward more CM-like and less PM-like (Fig. 5*A–D*; $n = 124$ neurons). As shown in the previous section, most of these neurons showed PM-selective responses at the 120° cross angle (85/124, 68.6%). This percentage decreased slightly to 62.9% at the 90° (78/124) and much more significantly to 19.4% (24/124) at the 60° cross angle. Correspondingly, the number of CM-selective responses increased from 0.8% at 120° (1/124) and 4% at 90° (5/124) to 25% at 60° (31/124), as well as the unclassified responses (30.6, 33.1, and 55.6% at the three cross angles, respectively). Overall, narrowing the plaid cross angle shrank the distribution of *z*-scores to be centered around a *z*-score difference (Zp − Zc) of 0 and increased the number of unclassified neurons. This is presumably because at smaller cross angles, the two tuning curves to the component gratings overlap substantially, making it more difficult to distinguish PM- and CM-selective responses. This is especially true for SC direction selective neurons, which have broad tuning curves (Inayat et al., 2015), while a similar trend has been observed in mouse V1 when comparing a narrow (60°) cross angle and wide (120°) cross angle plaid (Palagina et al., 2017).

We also examined the degree of direction selectivity at different cross angles (Fig. 5E–G), which showed a consistent pattern. The gDSI to single gratings was higher than that to each of the different cross angle plaids (120°, $p = 2.97 \times 10^{-5}$, z statistic = 4.17; 90°, $p = 2.89 \times 10^{-4}$, z statistic = 3.62; 60°, $p = 0.0037$, z statistic = 2.90; Wilcoxon test). On the other hand, the gDSI of gratings and plaids were significantly correlated at all cross angles (120°, $r^2 = 0.609$, $p = 1.20 \times 10^{-26}$; 90°, $r^2 = 0.637$, $p = 1.395 \times 10^{-32}$; 60°, $r^2 = 0.685$, $p = 2.35 \times 10^{-32}$). In other words, direction selective SC neurons predominantly showed selective responses to moving plaid patterns, and the vast majority of them were strongly PM selective and very few were CM selective at 120 and 90° cross angles.

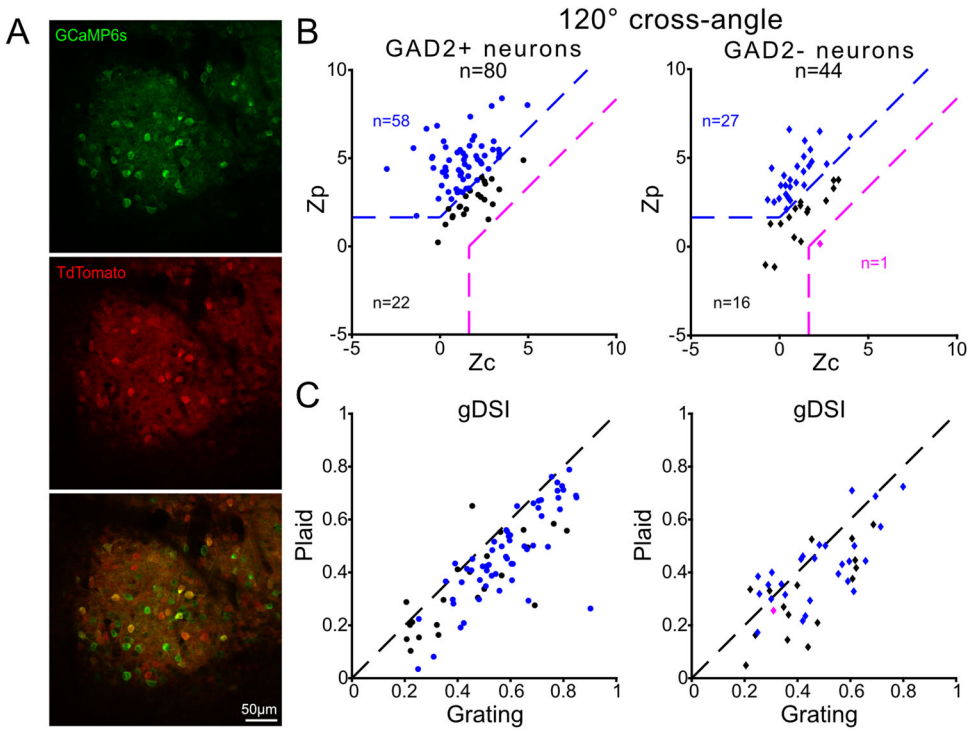

Figure 4. Both excitatory and inhibitory sSC neurons show pattern selective responses. ***A***, Two-photon images of neurons in the sSC labeled with GCaMP6s (green); GAD2$^+$ neurons are labeled with TdTomato (red). Scale bar: 50 μm. ***B***, Scatter plot of the *z*-score coefficients (Zp vs Zc) for putative inhibitory (left) and excitatory (right) SC neurons. ***C***, Scatter plot of gDSI for plaids versus drifting gratings for putative inhibitory (left) and excitatory (right) SC neurons. $n = 124/262$ neurons from two animals. Dashed lines represent 95% confidence threshold.

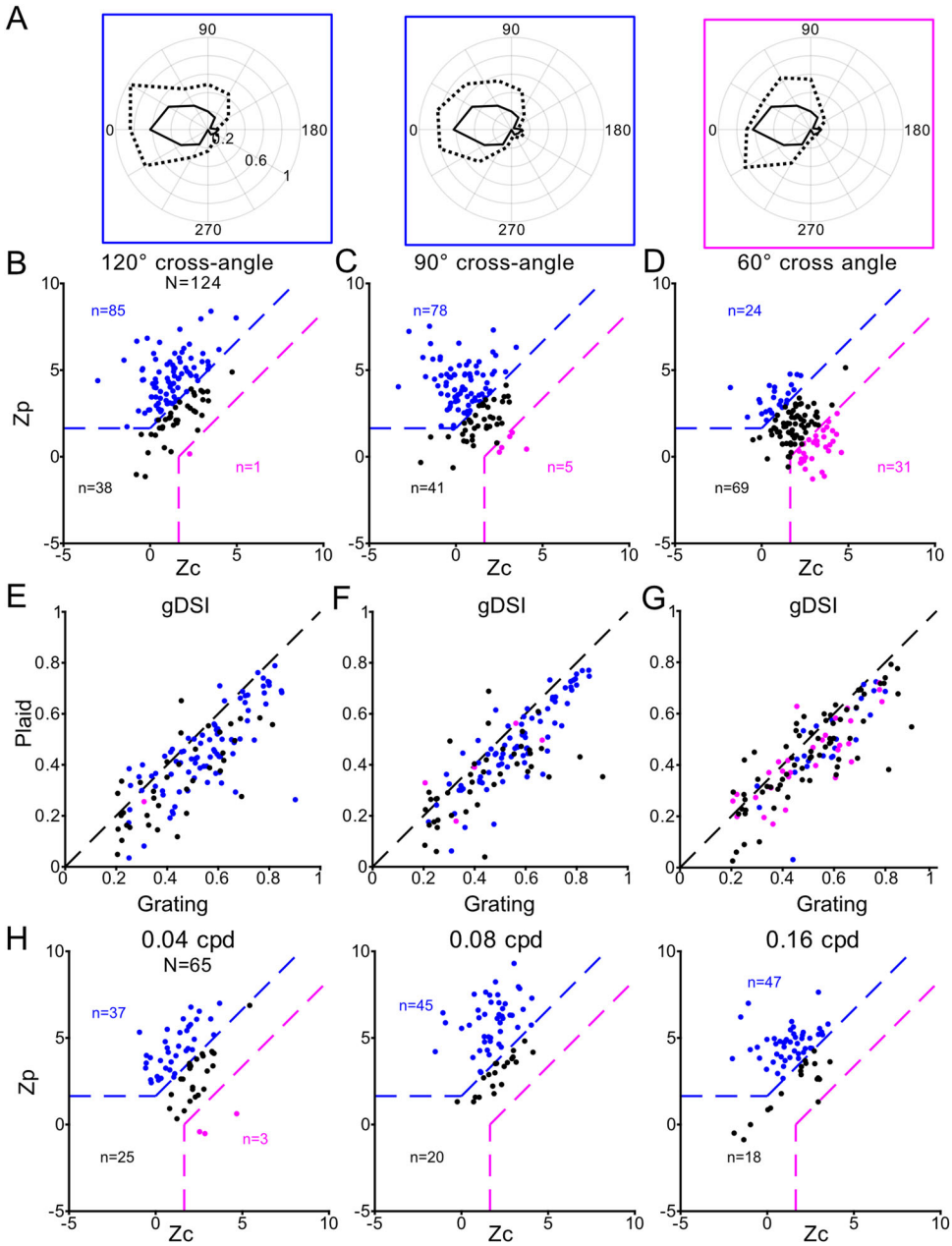

Figure 5. More sSC neurons show pattern selective responses to wider cross angle plaids. ***A***, Example tuning curves of a single SC neuron to drifting gratings (solid black line) and 120° (PM, left), 90° (PM, middle), and 60° (CM, right) cross angle plaids (dash black line). ***B***, Scatter plot of *z*-score coefficients (Zp vs Zc) for 120° plaids. ***C***, Same as in B but for 90° cross angle. ***D***, Same as in B and C but for 60° cross angle. ***E–G***, Scatter plots of gDSI for plaids versus drifting gratings for 120, 90, and 60° cross angle plaids. $n = 124/262$. All circles are colored according to *z*-score statistics classification (blue indicates PM, black indicates unclassified, and magenta indicates CM). Dashed lines represent the 95% confidence threshold. ***H***, Scatter plot of *z*-score coefficients (Zp vs Zc) for 120° plaids at three different spatial frequencies: left, 0.04 cpd; middle, 0.08 cpd; and right, 0.16 cpd. $n = 65$ neurons.

Lastly, we wanted to measure whether plaid classifications were stable across a range of spatial frequencies. We used three spatial frequencies: 0.04, 0.08, and 0.16 cpd with a plaid cross angle of 120°. No significant difference in plaid selectivity was observed to the change in spatial frequency (Fig. 5H).

Lack of predominantly PM-selective responses in DSGCs

SC direction selectivity is inherited from DSGCs in the retina (Shi et al., 2017). To determine whether the PM selectivity we observed in the SC might be also inherited from the retina, we first performed targeted loose-patch recordings from one subtype of posterior motion tuned On-Off DSGCs labeled in the DRD4-GFP transgenic mouse, which has been shown to specifically target the sSC, (Huberman et al., 2009). Grating and plaid parameters were optimized to maximally stimulate these neurons (see Materials and Methods for details). We presented 120°, 90°, and 60° cross angle plaids, and analyzed the partial correlation and *z*-score for the recorded cells (Fig. 6). At all the cross angles, at least half of the DSGCs were unclassified (28/34 at 120° cross angle, 82.4%; 22/41 at 90°, 53.7%; 12/18 at 60°, 66.7%). In contrast, very few neurons were clearly PM-selective (3/34 at 120° cross angle, 8.8%; 10/41 at 90°, 24.4%; 0/18 at 60°, 0%).

To characterize CM/PM selectivity across DSGC subtypes, we next utilized two-photon calcium imaging. We crossed Vglut2-Cre mouse lines with GCaMP6f reporter line to image

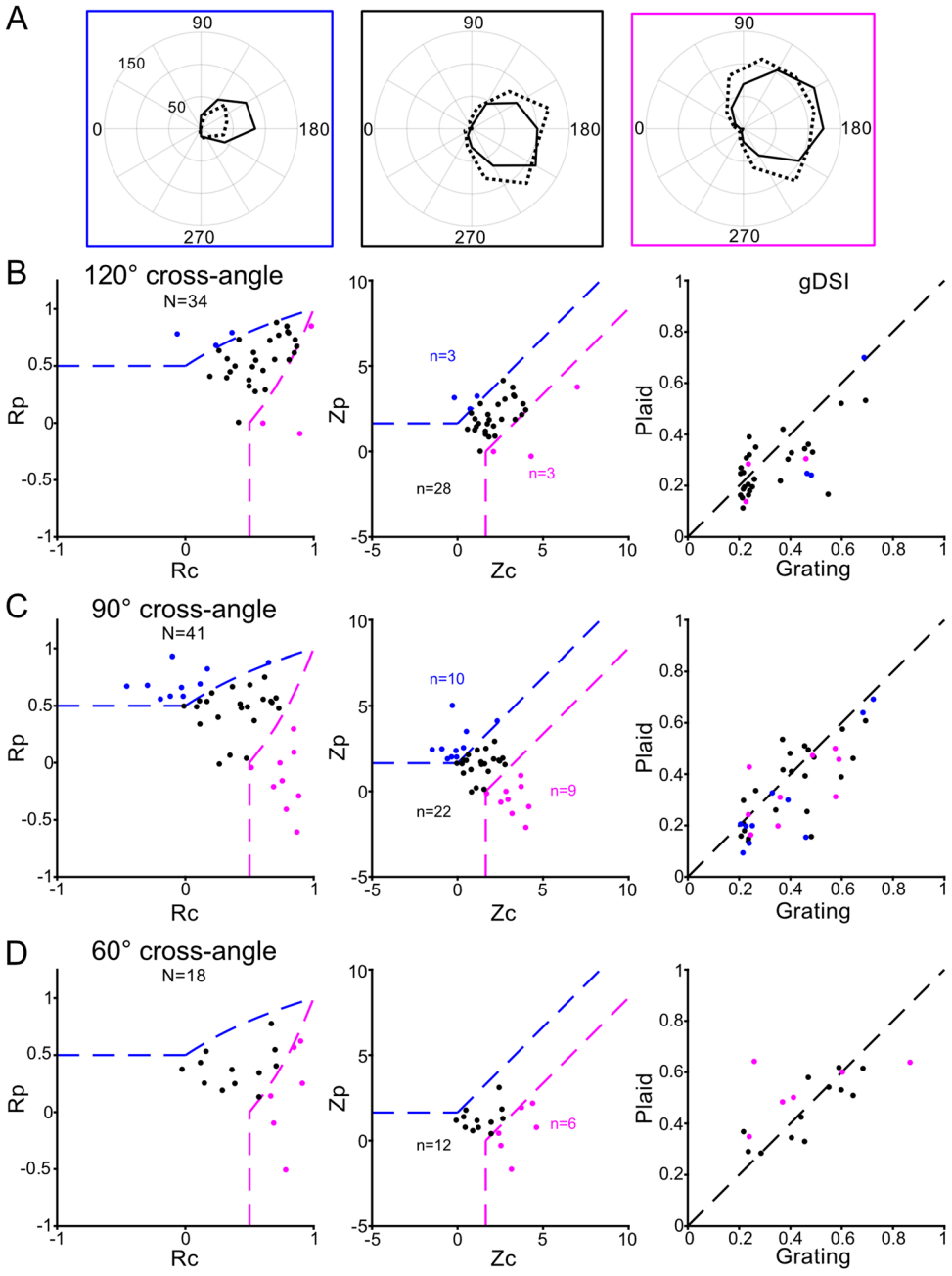

Figure 6. Direction selective retinal ganglion cells' responses to plaids. ***A***, Example tuning curves of loose-patch recorded Drd4-GFP + DSGCs. Solid black lines are the response to drifting gratings and the dotted lines are the responses to 90° plaids. Spikes/second ***B***, Left, scatter plot of partial correlation coefficients from DRD4+ DSGCs in response to 120° plaids. Middle, scatter plot of the *z*-score coefficients (Zp vs Zc). Right, scatter plot of gDSI for plaids versus drifting gratings. $n = 34$. ***C***, same as in ***A*** but for 90° plaids. $n = 41$. ***D***, Same as in ***A*** but for 60° plaids. $n = 18$. Dashed lines represent 95% confidence threshold. All circles are colored according to *z*-score statistics classification (blue indicates PM, black indicates unclassified, and magenta indicates CM). Dashed black line represents the line of equality.

all retinal ganglion cells (see Materials and Methods). To separate DSGC into On-Off and On classes, we showed stationary flashed spots in addition to gratings and plaids and characterized each cell's On and Off responses accordingly. In alignment with our electrophysiological recordings (Fig. 6), DSGCs showed mixed component and pattern selectivity across plaid angles (Fig. 7). On-Off DSGCs were mostly unclassified (71/112 at 120° cross angle, 63.4%; 35/76 46.1% at 90°; 27/46 58.7% at 60°). In both retina recording and imaging data, the proportion of PM-selective neurons varied with cross angles: 90° cross angle had the highest proportion (Fig. 7*C*, 32%, 25/76), followed by 120° cross angle (Fig. 7*B*, 25%, 28/112) and 60° cross angle (Fig. 7*D*, 13%, 6/46). In addition, we saw an increased proportion in CM-selective neurons as the plaid cross angle narrowed (13/112 at 120° cross angle, 11.7%; 17/76 22.4% at 90°; 13/46 28.3% at 60°). This angle-dependent effect is seen both in our retina electrophysiology and imaging data, as well as in SC responses.

Finally, we examined the proportion of PM- versus CM-selectivity of both retinal and SC neurons based on their preferred directions (Fig. 8). We color-coded based on their PM and CM selectivity, with each vector corresponding the neuron's preferred direction (angle of the vector) and gDSI (length; Fig. 8). The same trend was observed for all preferred directions – most SC neurons were PM selective in response to 120° and 90° cross

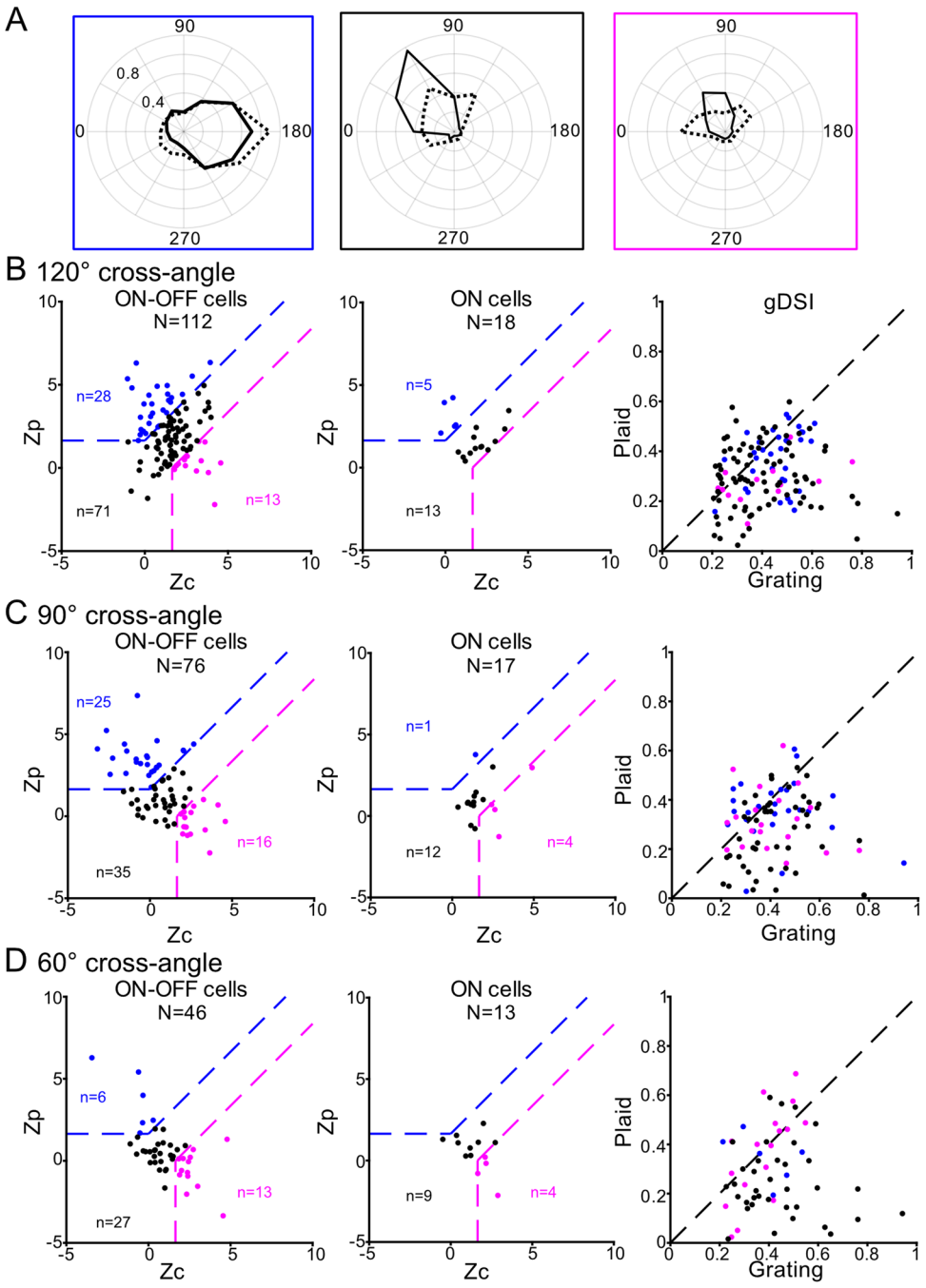

Figure 7. Calcium imaging of DSGCs responses to plaids. ***A***, Example tuning curves of DSGCs. Solid black lines are the responses to drifting gratings and the dotted lines are the responses to 120° plaids. ***B***, Left, scatter plot of the *z*-score coefficients (Zp vs Zc) for On-Off DSGCs, $n = 112$. Middle, scatter plot of the *z*-score coefficients (Zp vs Zc) for On DSGCs, $n = 18$. Right, scatter plot of gDSI for plaids versus drifting gratings for both groups. ***C***, same as in ***A***, but for 90° plaids. On-Off DSGCs, $n = 76$; On DSGCs, $n = 17$. ***D***, same as in A but for 60° plaids. On-Off DSGCs, $n = 46$; On DSGCs, $n = 13$.

angle plaids (Fig. 8*C*), whereas DSGCs were mostly unclassified regardless the preferred direction.

Together, these data indicate that while DSGCs show robust directional tuning to both drifting gratings and plaids, their responses are largely unclassified in terms of pattern- or component selectivity. Instead, pattern selectivity emerges in the SC in the retinocollicular pathway.

Mouse V1 responses to plaids

It is well established that neurons in mouse V1 are highly tuned for stimulus orientation or motion axis (Niell and Stryker, 2008; Liu et al., 2009; Tan et al., 2011; Lien and Scanziani, 2018; Barbera et al., 2022), and a few recent studies have examined their responses to type I plaids (Juavinett and Callaway, 2015; Palagina et al., 2017). Here, we examined V1 responses to plaids under the same experimental condition as the SC imaging. We performed in vivo imaging in five animals and collected visual responses from 667 V1 neurons to gratings and 90° plaids. 334 of those neurons passed our initial responsivity tests (Materials and Methods). Neurons in V1 were more orientation selective than direction selective (Fig. 9*A*), consistent with previous studies of mouse V1 (Niell and Stryker, 2008; Rossi et al., 2020). The gDSI and gOSI distribution of V1 neurons were very different from those of superficial SC (Fig. 9*B*; 90° plaid dataset, seven

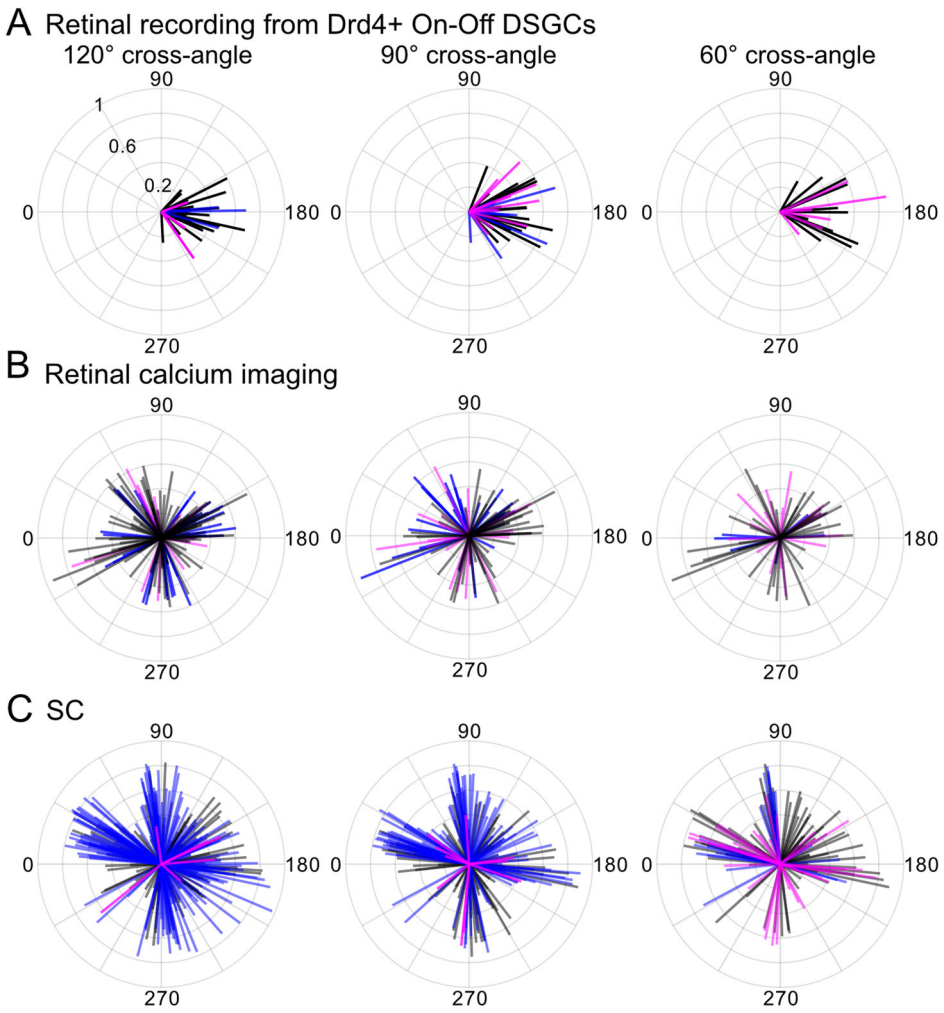

Figure 8. Comparison of DSGCs and sSC neurons responses to plaids. ***A***, Polar plots of loose-patch recorded DRD4-GFP + DSGCs showing their preferred direction (angle in the plot), gDSI (magnitude), and *z*-score statistics classification (blue indicates PM selective, black indicates unclassified, magenta indicates CM selective). From left to right: 120, 90, and 60°. ***B***, Same as in ***A***, but for a mixed population of ON-OFF and ON DSGCs measured by calcium imaging. ***C***, Same as in A but for sSC direction selective neurons that passed the selection criteria of max ΔF/F > 0.2 and gDSI > 0.2.

animals, 429 neurons), in that SC neurons skew toward higher gDSI values while overall having lower gOSI values compared to V1.

The response to plaids of these V1 neurons was also drastically different from those of SC neurons. Unlike in the SC, where the neuronal response magnitude and direction selectivity were highly correlated between grating and plaid responses, no such correlation was seen for V1 neurons (Fig. 9*C*,*D*). The already low V1 direction selectivity (gratings, gDSI = 0.14 ± 0.01) showed a further reduction when stimulated with plaids (plaids, gDSI = 0.08 ± 0.01; $r^2 = 0.135$, $p = 0.0002$; Fig. 9*D*). These data suggest that most V1 neurons would not be PM selective. To confirm this, we performed the plaid analysis according to adjusted partial correction and *z*-score values for more selective V1 neurons (Fig. 9*E*,*F*; max ΔF/F0 > 0.1 and gOSI > 0.2; the criteria was adjusted to accommodate the lower response magnitude of V1 neurons than SC neurons). Of the 101 selected neurons, the vast majority of plaid responsive neurons were unclassified (86/101, 85.2%), consistent with the low response magnitude and weak direction selectivity to plaids, as well as with previous reports (Juavinett and Callaway, 2015; Palagina et al., 2017). Of the remaining neurons, more showed CM-selective responses (12/101, 11.9%) than PM selective responses (3/101, 2.9%) in V1. Together, these data reveal a striking difference in complex motion processing among V1 and SC neuronal populations.

Transformation of pattern selectivity from the retina to the SC

Next, we explored what circuit mechanisms could potentially give rise to the emergence of prominent PM selectivity in the SC. Particularly, since direction selective SC neurons acquire their selectivity from converging excitatory inputs from DSGCs, we asked whether the same transformation algorithm underlying the retinal-SC responses to drifting gratings could predict the transformation of plaid responses. We built a linear–nonlinear model based on retinal and SC responses to drifting gratings (Fig. 10*A*, see Materials and Methods for details) to capture the nonlinearity of retina-SC transformation. This nonlinearity is best fitted with a sigmoidal function (Fig. 10*B*). We noted that the experimentally measured tuning width for drifting gratings in the retina is broader than that in the SC (Fig. 10*C*,*D*), indicating the sharpening effect of the nonlinearity of retina-SC transformation on SC directional tuning curves (Fig. 10*B*). We

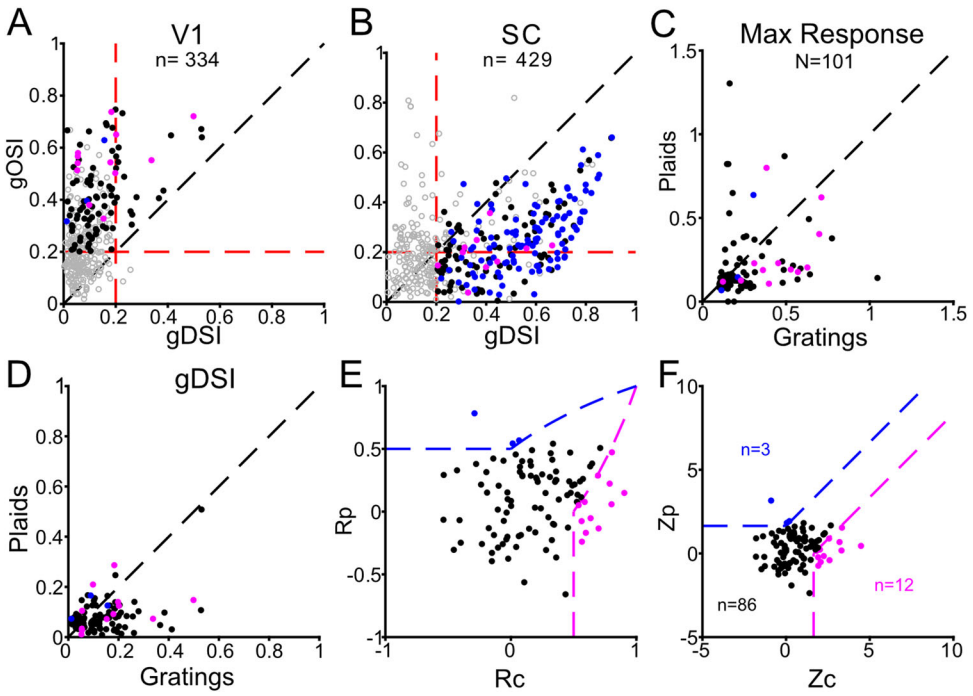

Figure 9. Comparison of SC and V1 neurons responses to 90° plaids. ***A***, Scatter plot of all the visually responsive V1 neurons showing gOSI veruss gDSI, $n = 334$ neurons from five animals. Dashed red lines show the gDSI (*x*-axis) or gOSI (*y*-axis) threshold of 0.2. ***B***, Same as in panel ***A***, but for recorded SC neurons. $n = 429$ neurons from 7 animals of the 90° plaid dataset. In ***A*** and ***B***, circles are colored according to *z*-score statistics classification (blue indicates PM selective, black indicates unclassified, magenta indicates CM selective, and open gray circles represent neurons that did not meet the selection criteria for plaid analysis. ***C***, Scatter plot of max responses to plaid versus drifting gratings for V1 neurons. ***D***, Scatter plot of gDSI for plaids versus drifting gratings for V1 neurons. ***E***, Scatter plot of partial correlation coefficients for V1 neurons. ***F***, Scatter plot of the *z*-score coefficients for V1 neurons. Colored dashed lines in ***E*** and ***F***, represent 95% confidence threshold. Black dashed line in ***A–D***, represents the line of equality. $n = 101/334$ neurons here are visually responsive V1 neurons that met the criteria: max $\Delta F/F > 0.1$ and gOSI > 0.2. All circles are colored according to *z*-score statistics classification (blue indicates PM, black indicates unclassified, and magenta indicates CM).

then feed the retinal plaid responses to the model to obtain simulated SC plaid responses.

To compare the relative selectivity of CM versus PM in experimental and simulated SC datasets, we used "pattern index", which is defined as the *z*-score difference between PM and CM (see Materials and Methods). More negative values of the pattern index indicate CM-selectivity and more positive values indicate PM selectivity. Consistent with earlier figures, experimentally measured pattern indices of DSGCs show a unimodal distribution that is centered around zero, indicating most retinal neurons are unclassified. Measured SC pattern indices also show a unimodal distribution that is right shifted toward PM selectivity (Fig. 10*E*). Simulated SC dataset shows a similar rightward shift of pattern index compared to the retina (Fig. 10*F*) and is closely matched to the pattern index distribution of the experimental SC data (Fig. 10*G*). Therefore, the same linear–nonlinear model can capture the transformation of retina-SC responses for both drifting gratings and plaids and recapitulates the rightward shift from unclassified DSGC plaid responses to PM-selective SC plaid responses (Fig. 10*H*).

Discussion

Plaid patterns are a useful stimulus to study how visual neurons encode complex motion. Any neuron that performs a spatiotemporal summation of the stimulus, like those found in cat (Gizzi et al., 1990) and primate V1 (Movshon et al., 1985), would necessarily respond to the component sinusoids (i.e., CM selective). If a neuron instead responds to the perceived PM, it provides evidence for a process that is substantially more advanced than a simple spatiotemporal summation. Here, we found that direction selective neurons in the SC are primarily PM selective, tuning more faithfully to the global motion of the plaid pattern than to the individual components. This is in marked contrast to how mouse V1 neurons respond to complex plaid motion: V1 cells were mostly orientation, instead of direction, selective for gratings and responded weakly to plaids. Classification using correlation analysis showed that most V1 cells were unclassified, and the few that could be classified were CM rather than PM. Our results support the notion that the SC is a predominant structure in computing and encoding complex motion, which may be associated with its functions in capturing moving preys (Hoy et al., 2016, 2019) and escaping from looming predators (Zhao et al., 2014; Evans et al., 2018; Zhou et al., 2019; Lee et al., 2020).

In contrast to SC neurons, the majority of DSGCs in the retina are not classified as PM selective. Their responses are rather similarly correlated to both CM- and PM- selective predictions and therefore labeled "unclassified". This effect is observed in both loose-patch recordings and calcium imaging, and in all On-Off DSGC subtypes. Such response pattern rules out a simple inheritance of PM selectivity from the retina to the SC. Several observations are worth noting. First, we did not see any clustering of pattern selectivity based on preferred direction in the retina or SC. This indicates that despite known differences in central projection patterns of DSGC subtypes (Kim et al., 2010; Kay et al., 2011), distributions of component and pattern selectivity are similar among subtypes. Second, the 120° cross angle, which generated the most dissimilar component and pattern predictions, did not parse out CM and PM responses any better than other cross angles in the retina. This gives further proof that retinal DSGCs are not linear "Fourier analyzers" like component cells in primate V1, and there exists nonlinearity within the retina

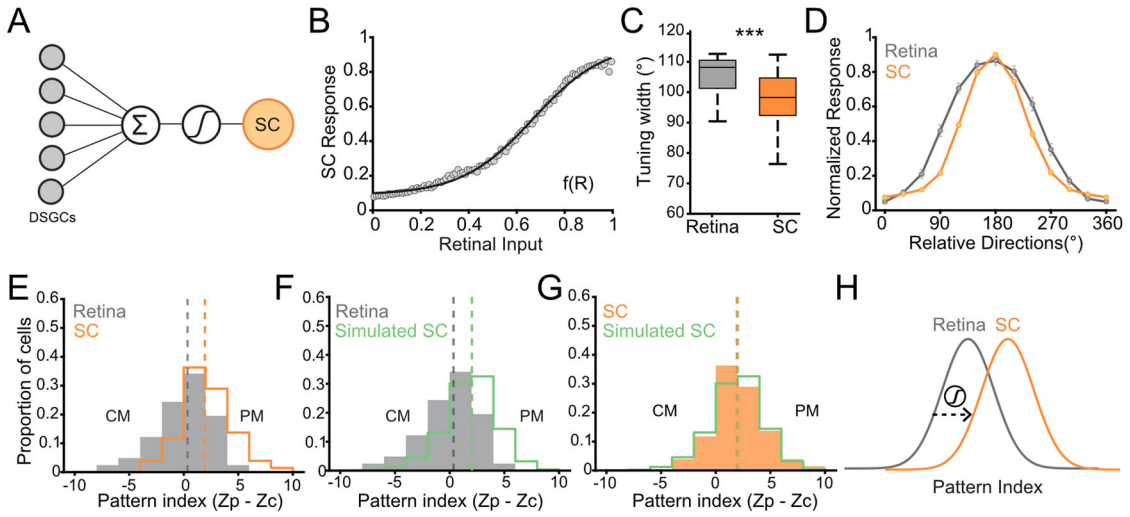

Figure 10. A linear–nonlinear model can explain the retina-SC transformation of plaid responses. ***A***, Schematic of the linear–nonlinear model. Normalized spiking responses from five similarly tuned direction-selective ganglion cells are first averaged and then transformed via a sigmoid function to produce the simulated response of an SC neuron to drifting gratings or plaids. ***B***, Mean SC responses plotted as a function of pooled retinal responses to drifting gratings. Black line, f(R), represents best-fit nonlinearity from 5,000 random draws of retinal inputs and SC response. Each time we randomly draw 5 DSGCs as input and 1 SC neuron as output. ***C***, Box plot of tuning widths (full width at half height of a von Mises fit, see Materials and methods) of 41 DRD4-GFP + DSGCs (gray) and 204 sSC cells' (orange) response to grating. Two-sample Kolmogorov–Smirnov test, $***p \ll 0.001$. ***D***, Normalized population-tuning curves for retinal (gray) and sSC (orange) neurons represented as the mean ± SEM. ***E***, Comparison of pattern index distribution between DSGCs (gray) and SC (orange) for 90° cross angle. Dashed line represents the median of each distribution. ***F***, Comparison of pattern index distributions between measured responses of DSGCs (gray) and 10,000 simulated SC responses (green). We simulated each SC grating and plaid response by applying the fitted nonlinearity, f(R), to the grating and plaid response of five randomly drawn DSGCs. Dashed line represents the median of each distribution. ***G***, Comparison of pattern index distributions between measured responses from 204 sSC neurons (orange) and 10,000 simulated SC neuron responses (green). Dashed line represents the median of each distribution. ***H***, Diagram showing that fitted nonlinearity can explain the shift in pattern index from retina to SC.

direction-selective pathway. Further studies will be needed to reveal the mechanisms of plaid encoding in the retina.

What circuit mechanisms might generate PM selectivity in the SC? Our modeling results suggest that the same nonlinearity applies to the retina-SC transformation of responses to both drifting gratings and plaids. For drifting gratings, this nonlinearity sharpens the direction tuning width from the retina to the SC. For plaids, the sharpening of tuning curves in the SC underlies the shift from unclassified retinal responses to the PM-selective SC responses. Exact sources of this nonlinearity are currently unknown, which may arise from multiple mechanisms. For example, directional tuning can be sharpened by spike thresholding and dendritic spikes (Oesch et al., 2005; Schachter et al., 2010; Harris and Dunn, 2023). Sharpening may also arise from nonlinear interactions of excitatory retinal inputs and local inhibition of SC circuitry. Future studies on the synaptic integration of SC neurons will provide further insights into the neural substrates underlying SC PM selectivity.

Studies in primate cortex led to a computational model to explain how area MT computes PM selectivity from CM-selective V1 inputs. The so-called "cascade model" implements a linear–nonlinear model on the nonlinear output of direction selective V1 neurons and can predict a full range of PM-selective, unclassified, and CM-selective responses seen in the MT (Simoncelli and Heeger, 1998; Rust et al., 2006). The model requires a convergence of V1 inputs tuned to a wide range of directions and the broadly tuned input to individual MT neurons is then suppressed by strong feedforward inhibition to maintain sharp selectivity for gratings and plaids of different cross angles.

There are important differences between the retinocollicular transformation and what is required in the V1-MT cascade model, making it an unlikely mechanism for the PM computation in the SC. First, the converging retinal input is not as broad as needed in the model. Our previous study in fact demonstrated that the retinal input is sharply tuned due to a precise convergence of similarly tuned DSGCs (Shi et al., 2017). Consistently, local inhibition in the SC is not needed to sharpen direction selectivity. Second and more importantly, the cascade model operates on inputs that are CM selective, which is not seen in the DSGCs responses to plaids. Instead, a diversity of responses was observed, and most DSGCs were unclassified. This is largely consistent with previous plaid studies of DSGCs from rabbit and salamander retina (Grzywacz and Amthor, 2007; Kühn and Gollisch, 2016). These properties of the retinocollicular transformation are taken into account by our linear–nonlinear model, which parsimoniously and accurately predicts the emergence of PM selectivity in the SC.

Finally, our V1 data show a similar distribution of motion selectivity compared to previous mouse studies (Juavinett and Callaway, 2015; Palagina et al., 2017). Where our data differed were in the overall proportion of highly direction selective neurons found in V1 (Fig. 8). Only 11.9% (12/101) of visually responsive V1 neurons in our data had a gDSI greater than 0.2. While in previous studies, using DSI >0.5 as a cutoff, Juavinett and Callaway (2015) found 19.6% and Palagina et al. (2017) found ~47% of V1 neurons to be direction selective. This discrepancy may be a result of animal state (awake vs anesthetized) and type of calcium indicator (GCaMP6 vs OGB-1). Our choice to threshold V1 neurons using gOSI instead of gDSI gave a better representation of the population of cells recorded from V1 (Niell and Stryker, 2008). Importantly, regardless of the selection criteria, the difference between V1 and SC in motion processing is clear. Our study thus highlights the importance of the SC in encoding PM and alludes to the nonlinear transformation from the retina to the SC underlying this computation.

References

Adelson EH, Movshon JA (1982) Phenomenal coherence of moving visual patterns. Nature 300:523–525.

Albright T, Stoner G (1995) Visual motion perception. Proc Natl Acad Sci U S A 92:2433–2440.

Baden T, Berens P, Franke K, Román Rosón M, Bethge M, Euler T (2016) The functional diversity of retinal ganglion cells in the mouse. Nature 529: 345–350.

Barbera D, Priebe NJ, Glickfeld LL (2022) Feedforward mechanisms of cross-orientation interactions in mouse V1. Neuron 110:297–311.e4.

Barchini J, Shi X, Chen H, Cang J (2018) Bidirectional encoding of motion contrast in the mouse superior colliculus. eLife 7:e35261.

Basso MA, May PJ (2017) Circuits for action and cognition: a view from the superior colliculus. Annu Rev Vis Sci 3:197–226.

Basso MA, Bickford ME, Cang J (2021) Unraveling circuits of visual perception and cognition through the superior colliculus. Neuron 109:918–937.

Brainard DH (1997) The psychophysics toolbox. Spat Vis 10:433–436.

Cang J, Savier E, Barchini J, Liu X (2018) Visual function, organization, and development of the mouse superior colliculus. Annu Rev Vis Sci 4:239–262.

Chen H, Savier EL, DePiero VJ, Cang J (2021) Lack of evidence for stereotypical direction columns in the mouse superior colliculus. J Neurosci 41: 461.

de Malmazet D, Kühn NK, Farrow K (2018) Retinotopic separation of nasal and temporal motion selectivity in the mouse superior colliculus. Curr Biol 28:2961–2969.e4.

Ellis EM, Gauvain G, Sivyer B, Murphy GJ (2016) Shared and distinct retinal input to the mouse superior colliculus and dorsal lateral geniculate nucleus. J Neurophysiol 116:602–610.

Elstrott J, Anishchenko A, Greschner M, Sher A, Litke AM, Chichilnisky EJ, Feller MB (2008) Direction selectivity in the retina Is established independent of visual experience and cholinergic retinal waves. Neuron 58:499–506.

Evans DA, Stempel AV, Vale R, Ruehle S, Lefler Y, Branco T (2018) A synaptic threshold mechanism for computing escape decisions. Nature 558:590–594.

Gale SD, Murphy GJ (2014) Distinct representation and distribution of visual information by specific cell types in mouse superficial superior colliculus. J Neurosci 34:13458–13471.

Gizzi MS, Katz E, Schumer RA, Movshon JA (1990) Selectivity for orientation and direction of motion of single neurons in cat striate and extrastriate visual cortex. J Neurophysiol 63:1529–1543.

Grzywacz NM, Amthor FR (2007) Robust directional computation in on-off directionally selective ganglion cells of rabbit retina. Vis Neurosci 24:647–661.

Harris SC, Dunn FA (2023) Asymmetric retinal direction tuning predicts optokinetic eye movements across stimulus conditions. eLife 12:e81780.

Hoy JL, Yavorska I, Wehr M, Niell CM (2016) Vision drives accurate approach behavior during prey capture in laboratory mice. Curr Biol 26:3046–3052.

Hoy JL, Bishop HI, Niell CM (2019) Defined cell types in superior colliculus make distinct contributions to prey capture behavior in the mouse. Curr Biol 29:4130–4138.e5.

Huberman AD, Wei W, Elstrott J, Stafford BK, Feller MB, Barres BA (2009) Genetic identification of an on-off direction-selective retinal ganglion cell subtype reveals a layer-specific subcortical map of posterior motion. Neuron 62:327–334.

Inayat S, Barchini J, Chen H, Feng L, Liu X, Cang J (2015) Neurons in the most superficial lamina of the mouse superior colliculus are highly selective for stimulus direction. J Neurosci 35:7992.

Juavinett AL, Callaway EM (2015) Pattern and component motion responses in mouse visual cortical areas. Curr Biol 25:1759–1764.

Kay JN, De la Huerta I, Kim I-J, Zhang Y, Yamagata M, Chu MW, Meister M, Sanes JR (2011) Retinal ganglion cells with distinct directional preferences differ in molecular identity, structure, and central projections. J Neurosci 31:7753–7762.

Kim I-J, Zhang Y, Meister M, Sanes JR (2010) Laminar restriction of retinal ganglion cell dendrites and axons: subtype-specific developmental patterns revealed with transgenic markers. J Neurosci 30:1452.

Kühn NK, Gollisch T (2016) Joint encoding of object motion and motion direction in the salamander retina. J Neurosci 36:12203.

Lee KH, Tran A, Turan Z, Meister M (2020) The sifting of visual information in the superior colliculus. eLife 9:e50678.

Lien AD, Scanziani M (2018) Cortical direction selectivity emerges at convergence of thalamic synapses. Nature 558:80–86.

Liu B, Li P, Li Y-T, Sun YJ, Yanagawa Y, Obata K, Zhang LI, Tao HW (2009) Visual receptive field structure of cortical inhibitory neurons revealed by two-photon imaging guided recording. J Neurosci 29:10520.

Liu Y, Savier EL, DePiero VJ, Chen C, Schwalbe DC, Abraham-Fan R-J, Chen H, Campbell JN, Cang J (2023) Mapping visual functions onto molecular cell types in the mouse superior colliculus. Neuron 111:1876–1886.e5.

Mauss AS, Vlasits A, Borst A, Feller M (2017) Visual circuits for direction selectivity. Annu Rev Neurosci 40:211–230.

Movshon JA, Newsome WT (1996) Visual response properties of striate cortical neurons projecting to area MT in macaque monkeys. J Neurosci 16:7733.

Movshon JA, Adelson EH, Martin GS, Newsome WT (1985) The analysis of moving visual patterns. In: *Pattern recognition mechanisms* (Chagas C, Gattass R, Gross C, eds), pp 117–151, 1st edn. Vatican, Rome, Italy: Springer Berlin, Heidelberg. Experimental Brain Research Series.

Niell CM, Stryker MP (2008) Highly selective receptive fields in mouse visual cortex. J Neurosci 28:7520.

Nishida S, Kawabe T, Sawayama M, Fukiage T (2018) Motion perception: from detection to interpretation. Annu Rev Vis Sci 4:501–523.

Oesch N, Euler T, Taylor WR (2005) Direction-selective dendritic action potentials in rabbit retina. Neuron 47:739–750.

Palagina G, Meyer JF, Smirnakis SM (2017) Complex visual motion representation in mouse area V1. J Neurosci 37:164.

Pasternak T, Tadin D (2020) Linking neuronal direction selectivity to perceptual decisions about visual motion. Annu Rev Vis Sci 6:335–362.

Quaia C, Optician LM, Cumming BG (2016) A motion-from-form mechanism contributes to extracting pattern motion from plaids. J Neurosci 36:3903.

Quaia C, Kang I, Cumming BG (2022) Pattern motion direction Is encoded in the population activity of macaque area MT. J Neurosci 42:9372.

Rodman HR, Albright TD (1989) Single-unit analysis of pattern-motion selective properties in the middle temporal visual area (MT). Exp Brain Res 75:53–64.

Rossi LF, Harris KD, Carandini M (2020) Spatial connectivity matches direction selectivity in visual cortex. Nature 588:648–652.

Rust NC, Mante V, Simoncelli EP, Movshon JA (2006) How MT cells analyze the motion of visual patterns. Nat Neurosci 9:1421–1431.

Savier EL, Chen H, Cang J (2019) Effects of locomotion on visual responses in the mouse superior colliculus. J Neurosci 39:9360.

Schachter MJ, Oesch N, Smith RG, Taylor WR (2010) Dendritic spikes amplify the synaptic signal to enhance detection of motion in a simulation of the direction-selective ganglion cell. PLOS Comput Biol 6:e1000899.

Shi X, Barchini J, Ledesma HA, Koren D, Jin Y, Liu X, Wei W, Cang J (2017) Retinal origin of direction selectivity in the superior colliculus. Nat Neurosci 20:550–558.

Simoncelli EP, Heeger DJ (1998) A model of neuronal responses in visual area MT. Vision Res 38:743–761.

Smith MA, Majaj NJ, Movshon JA (2005) Dynamics of motion signaling by neurons in macaque area MT. Nat Neurosci 8:220–228.

Tan AY, Brown BD, Scholl B, Mohanty D, Priebe NJ (2011) Orientation selectivity of synaptic input to neurons in mouse and cat primary visual Cortex. J Neurosci 31:12339.

Tohmi M, Tanabe S, Cang J (2021) Motion streak neurons in the mouse visual cortex. Cell Rep 34:108617.

Vaney DI, Sivyer B, Taylor WR (2012) Direction selectivity in the retina: symmetry and asymmetry in structure and function. Nat Rev Neurosci 13: 194–208.

Wang HX, Movshon JA (2016) Properties of pattern and component direction-selective cells in area MT of the macaque. J Neurophysiol 115: 2705–2720.

Wei W (2018) Neural mechanisms of motion processing in the mammalian retina. Annu Rev Vis Sci 4:165–192.

Zhao X, Liu M, Cang J (2014) Visual cortex modulates the magnitude but not the selectivity of looming-evoked responses in the superior colliculus of awake mice. Neuron 84:202–213.

Zhou Z, et al. (2019) A VTA GABAergic neural circuit mediates visually evoked innate defensive responses. Neuron 103:473–488.e6.